Turk J Phys
26 (2002) , 133 – 155.

On Numerical Simulations of Composite Dielectrics in Thermally Stimulated Conditions*

Enis TUNCER,† Stanisław M. GUBAŃSKI
High Voltage Division, Department of Electric Power Engineering,
Chalmers University of Technology, 412 96 Gothenburg-SWEDEN
e-mail: enis.tuncer@elkraft.chalmers.se

Received 15.12.2000

Abstract

A binary composite system with particulated inclusions was considered. First, thermally stimulated depolarization (TSD) currents of the system were simulated by altering different parameters of the TSD current equation, *i.e.*, intrinsic dielectric properties of constituents, conductivity of inclusions, heating rate and activation energy of inclusion conductivity and shape of inclusions. Two different methods of finding the activation energy of TSD processes from the simulated TSD currents were discussed. Second, we have included the Monte Carlo technique by assuming that the shape factor of inclusions were distributed. These simulations have shown that if the inclusions were distorted spheres, the resulting TSD currents were identical. Finally, since the classical calculations have neglected the inclusion-inclusion interactions, the finite element method (FEM) was used to include the influence of local fields (mutual interaction of inclusions). The dielectric responses of two-dimensional systems at isothermal conditions were calculated by the FEM, and later, the TSD currents were estimated with the FEM results by assuming a constant activation energy for the relaxation processes. The comparison of the obtained results has shown that the influence of micro-structure and mutual interaction of particles should be included in the modeling considerations.

Key Words: Dielectrics, composite materials, thermally stimulated depolarization current.

1. Introduction

Predicting and understanding the dielectric properties of a medium formed from a mixture of different dielectric materials has been a challenging problem of both theoretical and practical importance. These heterogeneous systems composed of two or more phases show different conductive and dielectric properties depending on the electrical properties of phases [1, 2, 3]. Even the geometrical shapes [4] and arrangements of inclusions [5, 6] play an important role in the electrical properties of composites.

One of the techniques to study the dielectrical properties of materials is the thermally stimulated polarization or depolarization (TSD) current method [7, 8, 9]. In this technique, a material is polarized by applying an uniform and constant electric field E at an elevated temperature, then the material is cooled down in the applied field in order to freeze the polarization. Afterwards the depolarization current is recorded under a short-circuit condition while the sample is linearly-heated. The depolarization process results as a current in the external circuit when the frozen polarization is thermally activated.

*Supported by the ELIS program of the Swedisk Foundation for Strategic Research (SSF).
†To whom correspondence should be addressed

The TSD current of a composite is influenced by the micro-structure of the mixture as well as the applied voltage and the heating rate. In the simulations, a binary composite system composed of non-interacting conductive ellipsoidal inclusions in an insulating matrix was considered [4]. A similar approach was presented by Vila et al. [10] where the TSD current of a mixture containing inclusions of ellipsoidal shapes were studied.

When two media are put into contact (forming an interface) and an electric field is applied, due to the differences between the ratios of the electrical properties (conductivity and permittivity) charge polarization occurs at the interface. This polarization is called 'Maxwell-Wagner' or interfacial polarization [11, 12]. The dielectric response of the composite material with such polarization $\varepsilon(\omega) = \varepsilon'(\omega) - \imath\varepsilon''(\omega)$ can be written as follows in the form of a Debye model [13],

$$\begin{aligned} \varepsilon'(\omega) =& \epsilon + \frac{\Delta\varepsilon}{1+\omega^2\tau^2} \\ \varepsilon''(\omega) =& \frac{\Delta\varepsilon\omega\tau}{1+\omega^2\tau^2}, \end{aligned} \tag{1}$$

where ϵ is the dielectric permittivity at optical frequencies $\Delta\varepsilon$ is the dielectric strength of the interfacial polarization, and τ is the relaxation time. Sillars [4] has introduced ellipsoidal inclusions, and has studied the dielectric behavior of these systems when the matrix medium was insulating ($\sigma_1 \ll \sigma_2$). The dielectric properties of such systems has been given by [4, 14] as

$$\begin{aligned} \epsilon =& \varepsilon_1 \left[1 + q\frac{n(\varepsilon_2 - \varepsilon_1)}{\varepsilon_1(n-1)+\varepsilon_2}\right] \\ \Delta\varepsilon =& \frac{q}{1-q}\frac{n^2\varepsilon_1^2}{(n-1)\varepsilon_1 + \varepsilon_2 - q(\varepsilon_2 - \varepsilon_1)} \\ \tau =& \frac{(n-1)\varepsilon_1 + \varepsilon_2}{\sigma_2}. \end{aligned} \tag{2}$$

Here, ε_1 is the dielectric permittivity of the matrix medium, and ε_2 and σ_2 are the dielectric permittivity and ohmic conductivity of the ellipsoidal inclusions, respectively. The parameters n and q are the shape factor for the inclusions and the volume fraction of the inclusions, respectively.

When the TSD currents of the composites are considered, the conductivity σ_2 in Eq. (2) can be assumed to temperature T dependent and Arrhenius activated with an activation energy W and a pre-exponential factor σ_0 as

$$\sigma_2 = \sigma_0 \exp\left(-\frac{W}{k_B T}\right). \tag{3}$$

Here, k_B is the Boltzmann constant, $k_B = 8.6174 \times 10^{-5}$eV/K. Then, the TSD current $j(T)$ is expressed as [7, 8, 9]

$$j(T) = \frac{P_0}{\tau(T)} \exp\left\{-\int_0^T \left[\frac{dT}{\mathcal{B}\tau(T)}\right]\right\} \tag{4}$$

where $\tau(T)$ is the temperature dependent relaxation time which is obtained by inserting Eq. (3) in Eq. (2). The other two parameters in Eq. (4), P_0 and $\mathcal{B}$, are the total sample polarization, and the linear heating rate in the experiments, respectively. The total polarization P_0 is

$$P_0 = \Delta\varepsilon E, \tag{5}$$

where E is the constant applied field. In the simulations, the composite systems were considered to be totally polarized, $P_0 =$ constant.

In this investigation, not only the shape factor but other physical parameters influencing the TSD current, *e.g.*, dielectric permittivities of the media, conductivity of the inclusions, activation energy of the conductivity etc. were explored. However, by altering the dielectric properties of phases and shapes of the inclusion

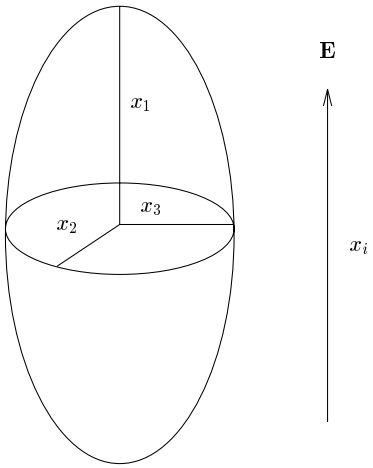

Figure 1. Ellipsoidal inclusion considered in the simulations.

particles, the dielectric strength $\Delta\varepsilon$ of the composite system changes that which was temperature independent in the calculations. The dielectric properties of a system with arbitrary ellipsoidal inclusions are given in Eq. (2) with a shape parameter, n. The n-value can be obtained for different directions, as illustrated in Fig. 1, and is given by [4, 14]

$$n_i = \frac{2}{x_1 x_2 x_3 \mathcal{L}_i}, \tag{6}$$

where subscript i denotes the desired axis-direction and

$$\mathcal{L}_i = \int_0^\infty \frac{d\zeta}{\left[(x_i^2+\zeta)^2(x_1^2+\zeta)(x_2^2+\zeta)(x_3^2+\zeta)\right]^{1/2}}. \tag{7}$$

The value of $\mathcal{L}_i$ is between 1 and infinity, $1 < \mathcal{L}_i < \infty$. The index i indicates the shape factor in that axis-direction.

For needle-like shapes parallel to the field direction, n-values are larger than 3. For spherical inclusions, the shape factor n_i is 3. For cylinderical inclusions, if the cylinder axis is perpendicular to the applied field, shape factor is 2. And if large disks perpendicular to the applied field are considered, the shape factor is 1.

2. Simulations of TSD current

The present work begins with the shape of inclusions was assumed to be identical and spherical, $n = 3$. The dielectric permittivity values of the host medium and inclusions were $\varepsilon_1 = 2$ and $\varepsilon_2 = 10$, respectively. The conductivity of the inclusions was taken to be Arrhenius activated, and the matrix phase was considered to be a perfect dielectric without any temperature dependent parameters, $\sigma_1 = 0$. The concentration of the inclusions, q, was 0.1 which is low enough to neglect the mutual interaction of inclusions. The applied field E, pre-exponential factor for conductivity σ_0, activation energy of the conductivity W and the heating rate were 10^4 V/m, 100 S/m, 0.7 eV and 0.1 K/s, respectively. The TSD current-response calculated according to Eq. (4) with these parameters is shown in Fig. 2. This response was considered as a reference TSD current for the later simulations. The peak-temperature T_p in which the current maximum is achieved was ~ 255 K, and the maximum current value $\max[j(T)] = j(T_p)$ was 43 pA.

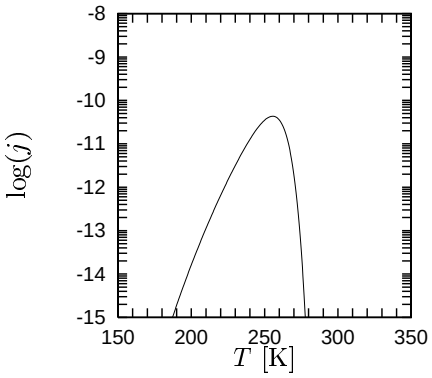

Figure 2. The reference TSD current curve.

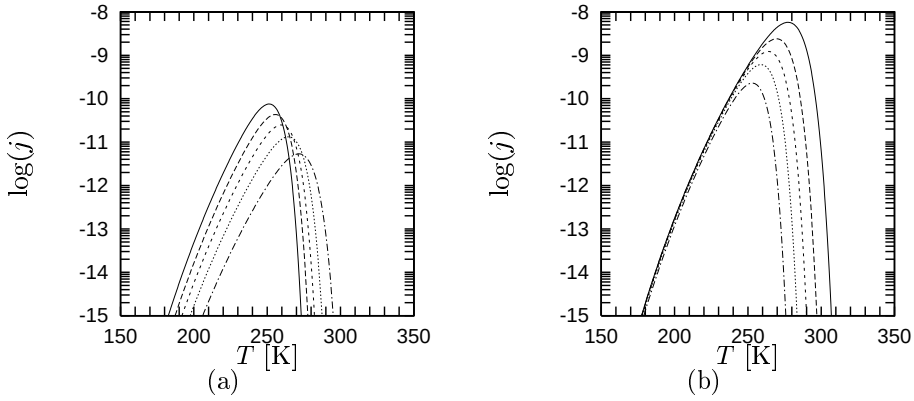

Figure 3. TSD currents of different $\mathcal{R}_\varepsilon$ cases. (a) $\mathcal{R}_\varepsilon < 1$ and (b) $\mathcal{R}_\varepsilon > 1$. The $\mathcal{R}_\varepsilon$-values increase with incresing temperature.

2.1. Intrinsic electrical properties of phases

The dielectric permittivity of the phases $\varepsilon_{1,2}$ were chosen such that the ratio of the dielectric permittivities $\mathcal{R}_\varepsilon$ was between 0.02 and 50. To achive these values, first the dielectric permittivity of the matrix ε_1 was kept constant at $\varepsilon_1 = 2$, and the dielectric permittivity of the inclusions were taken from an array of values, $\varepsilon_2 = [4, 10, 20, 40, 100]$. Later, the same procedure was repeated in which the dielectric permittivity of the inclusions ε_2 was kept constant at $\varepsilon_2 = 2$, and the same values were used for the permittivity of the matrix ε_1.

The results are displayed in Fig. 3. It was remarkable that when $\mathcal{R}_\varepsilon = \varepsilon_1/\varepsilon_2 < 1$ the TSD current curves had the similar width but decreasing in amplitudes for decreasing $\mathcal{R}_\varepsilon$ (Fig. 3a). The peak-temperature of TSD current T_p, moved to higher temperatures as the $\mathcal{R}_\varepsilon$ became smaller. When the $\mathcal{R}_\varepsilon > 1$ cases were taken into consideration, which are pre sented in Fig. 3b, first in contrast to $\mathcal{R}_\varepsilon < 1$ cases, the maximum current value $j(T_p)$ increased with increasing $\mathcal{R}_\varepsilon$-values. When the dielectric permittivity of the inclusions were lower than that of the matrix phase, it was not possible to separate the influence of the inclusions in the TSD current curves. When the temperature values were lower than 230 K, whereas, the influence of the dielectric permittivities were significant at the higher temperature-side of the spectra.

Dependencies of maximum current $j(T_p)$ on peak-temperature T_p are shown in Fig. 4a. The temperature range in which the peak could be found was about $\sim$ 25 K, from 250 K to 275 K, showing two distinct behaviors. First, $j(T_p)$-values could not be expected below $\sim$ 250 K shown in Fig. 4b). Secondly, both figures showed U-shape behavior in semi-logarithmic plots. It was clear that the influence of $\mathcal{R}_\varepsilon$ formed two

regions where the $\log[j(T_p)]$-points were placed.

Finally, if the change in $j(T_p)$ as a function of the $\mathcal{R}_\epsilon$ were considered, the shape of the dependency is linear-like in log-log plot, (see Fig. 5). However, the linearity was slightly deviated for the cases when $\mathcal{R}_\epsilon < 1$.

2.2. Pre-exponential factor of the conductivity

The pre-exponential factor of conductivity σ_0 in Eq. (3) was altered to obtain respective TSD currents. The activation energy W in the equation was kept constant. The σ_0-values were taken between 50 S/m and 500 S/m. The calculated TSD currents are presented in Fig. 6. The pre-exponential factor σ_0 slightly affected the shape of TSD currents and their peak current $j(T_p)$ as well as the peak temperature T_p but not as ambiguously as the intrinsic dielectric properties did. All the curves had similar shapes. The TSD currents were influenced only when the $\sigma_0 < 250$ S/m (Fig. 6a).

Dependence of $j(T_p)$ on T_p is plotted for altered σ_0 in Fig. 7a. The behavior was nearly-constant in semi-logarithmic scale, showing no correlation between these parameters. The $j(T_p)$-values also had a similar behavior with increasing pre-exponential factor σ_0 as presented in Fig. 7b. Moreover, the range of obtained T_p-values was ~ 15 K. When the pre-exponential factor of conductivity of the inclusions σ_0 was increased, the TSD current peak position T_p appeared at a lower temperature (see Fig. 8). But, when the region 250 S/m $< \sigma_0 <$ 500 S/m was considered, the change was smaller in amplitude than in the other region 50 S/m $< \sigma_0 <$ 250 S/m. The T_p-values decreased non-linearly converging at 240 K with increasing pre-expoential factor σ_0.

2.3. Heating rate

In TSD current experiments, the heating rate $\mathcal{B}$ can be adjusted. The effect of this parameter on the TSD current was considered and the calculated TSD currents are presented in Fig. 9. In the calculations, the $\mathcal{B}$-values were as follows:

$$\mathcal{B} = [0.01, 0.03, 0.06, 0.1, 0.15, 2, 3, 5, 1, 2] \text{ K/s}.$$

It was clear that an increase in heating rate increased the depolarization current, and the peak value of the current appeared at a higher temperature. Although the curves looked different in shape, the integral of the current with respect to time, $\int j(T)dt$, should be equal to the total polarization value. The TSD currents showed similar characteristics where all the curves had the same initial raising stage. Only the shape of TSD current became wider with increasing heating rate $\mathcal{B}$ which influenced the T_p-values. This behavior is shown Fig. 10. The relationship between T_p and $j(T_p)$ for altered $\mathcal{B}$-values was linear in semi-logarithmic scale. The range of the peak temperature obtained in this simulation was between 245 K and 280 K.

The activation energy of a process W may be obtained by performing measurements with different $\mathcal{B}$-values, then the activation energy W can be expressed as [15]

$$W = \frac{k_B T_{p_1} T_{p_2}}{T_{p_2} - T_{p_1}} \ln \frac{\mathcal{B}_2 T_{p_1}^2}{\mathcal{B}_1 T_{p_2}^2}. \tag{8}$$

The calculated activation energy values are presented in Fig. 11a. The values were estimated using Eq. (8) where combination of ten different heating rate values $\mathcal{B}$ together with their peak temperatures T_p were used. Taking two of the $\mathcal{B}$ and T_p-values at a time, and inserting them into Eq. (8), 45 different activation energy values were calculated. All of them except one were lower than the actual assigned activation energy, $W = 0.7$ eV. The mean value of the activation energies $\langle W \rangle$ was equal to 0.65 eV with standard deviation ± 0.01 eV. Another way to calculate the activation W was to plot the logarithm of the TSD current as a function of inverse normalized temperature, and to check the slope of the region where temperature is lower than peak temperature $T < T_p$ which is displayed in Fig. 11b. The slope is, then, equal to the activation energy W. The activation energy estimates were $W = 0.71$ eV, which was close to the originally assigned activation energy within 2% error. applicable when there exists only one activation energy. simulations, when the slope of the natural logarithm of the TSD current was check the actual activation energy was slightly deviated from the assigned one.

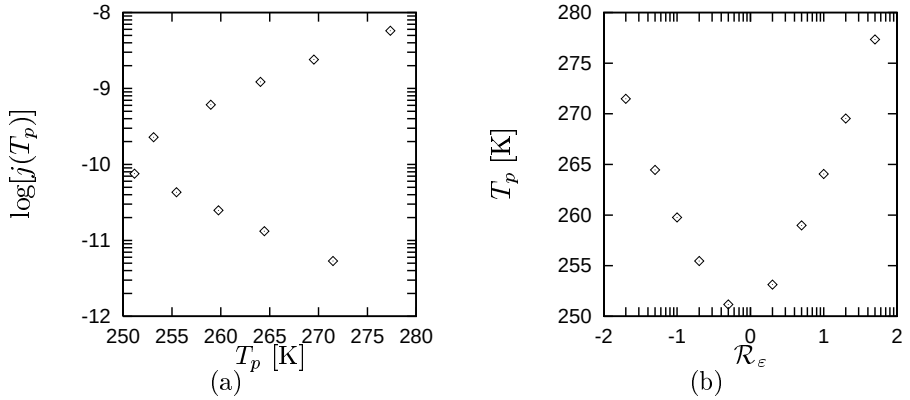

Figure 4. (a) Maximum current $j(T_p)$ as a function of its position in the temperature-axis T_p and (b) T_p as a function of $\mathcal{R}_\varepsilon$.

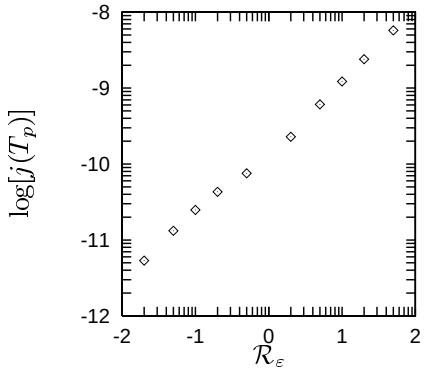

Figure 5. Change of maximum current value $j(T_p)$ as a function of dielectric permittivity ratios $\mathcal{R}_\varepsilon$.

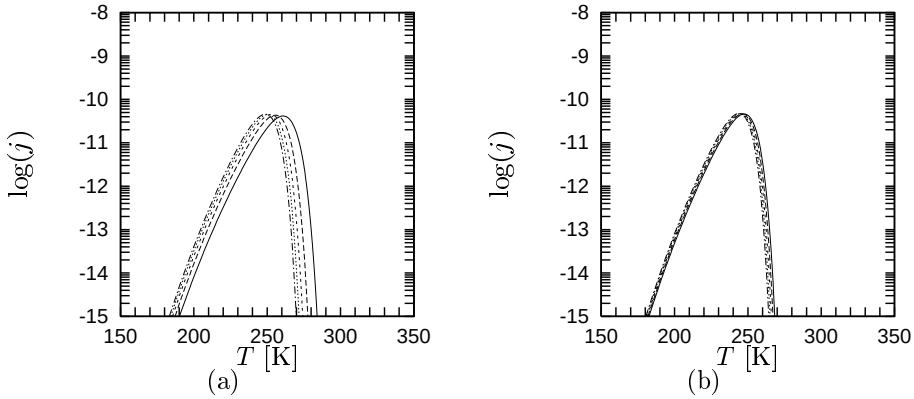

Figure 6. TSD current as a function temperature for different σ_0 values (a) when $50 < \sigma_0 < 250$ S/m and (b) $250 < \sigma_0 < 500$ S/m. The curves moved to lower temperatures for increasing σ_0.

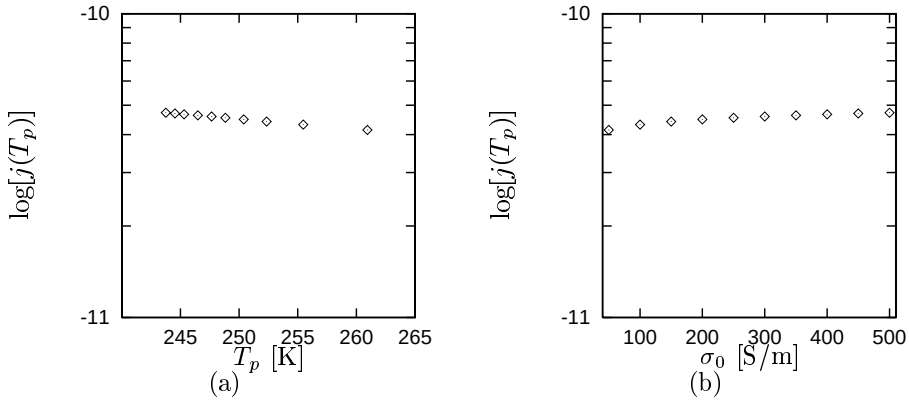

Figure 7. (a) Maximum current $j(T_p)$ as a function of its position in the temperature-axis T_p (b) $j(T_p)$ as a function of pre-exponential factor σ_0.

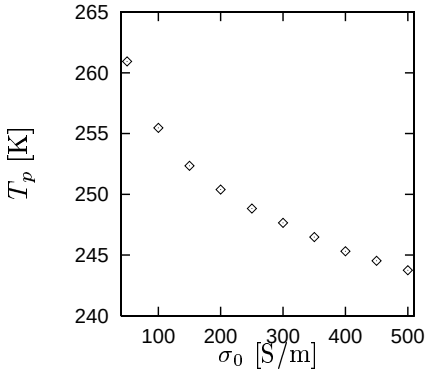

Figure 8. Change of peak temperature value T_p as a function of pre-exponential factor of conductivity σ_0 of phases.

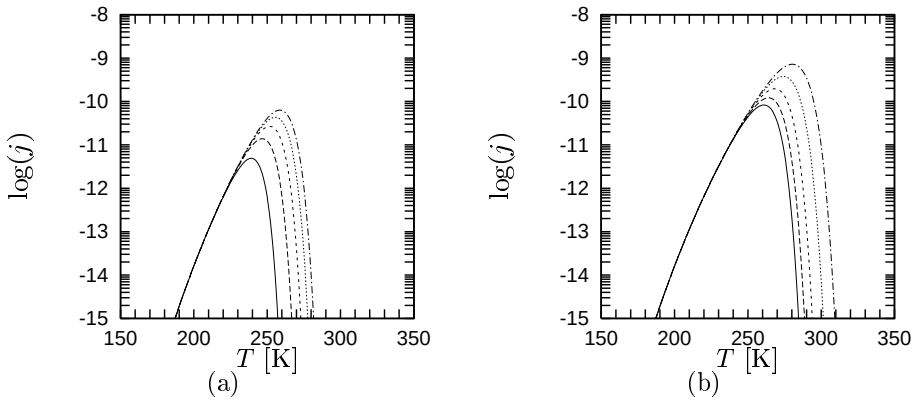

Figure 9. TSD current as a function temperature for different heating rate $\mathcal{B}$ values (a) when $\mathcal{B} = [0.01, 0.03, 0.06, 0.1, 0.15]$ K/s and (b) $\mathcal{B} = [0.2, 0.3, 0.5, 1.0, 2.0]$ K/s. The curves move to higher temperatures with increasing $\mathcal{B}$.

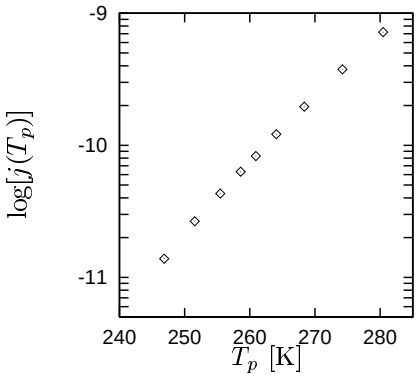

Figure 10. Maximum current value $j(T_p)$ of a TSD current and its position in the temperature axis T_p for different values of σ_0.

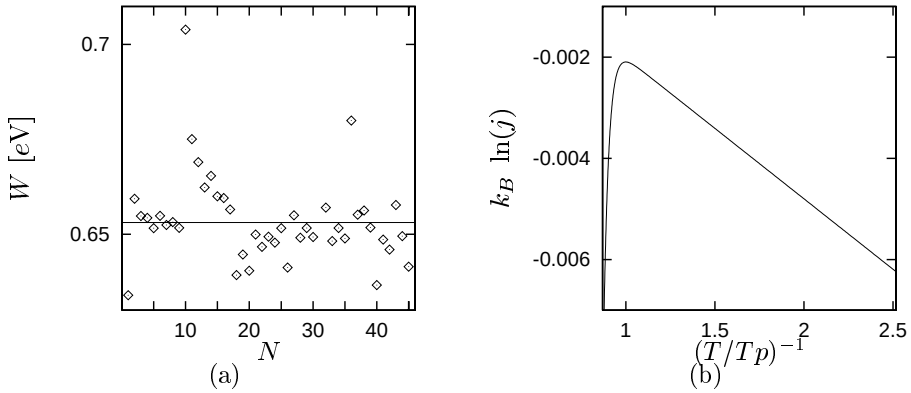

Figure 11. Activation energies calculated for the set of heating rates $\mathcal{B}$. N presents the set number, and the solid-line is the mean activation energy value $\langle W \rangle = 0.65$ eV with standard deviation of 0.01 eV. (b) Boltzmann constant times the natural logarithm of TSD current $k_B \ln[j(T)]$ as a function of inverse normalized temperature T_p/T. The slope of the line is 0.71 eV for $T_p/T > 1$.

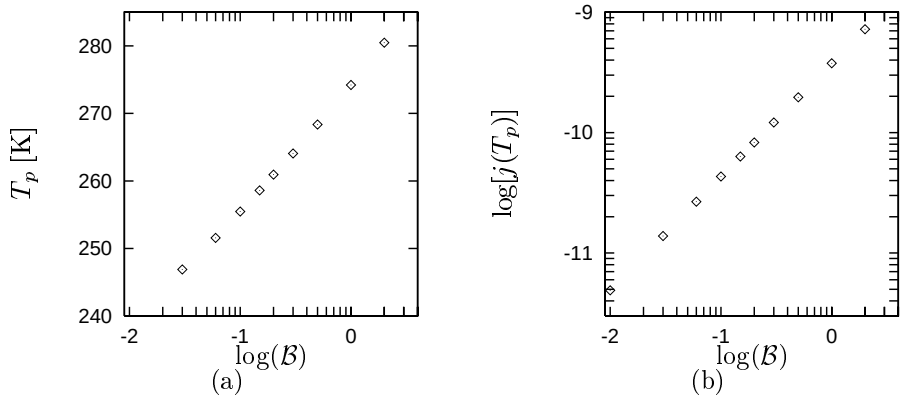

Figure 12. (a) Change in peak temperature T_p as a function of heating rate $\mathcal{B}$. (b) Maximum current $j(T_p)$ as a function of its position in the temperature-axis T_p for altered $\mathcal{B}$.

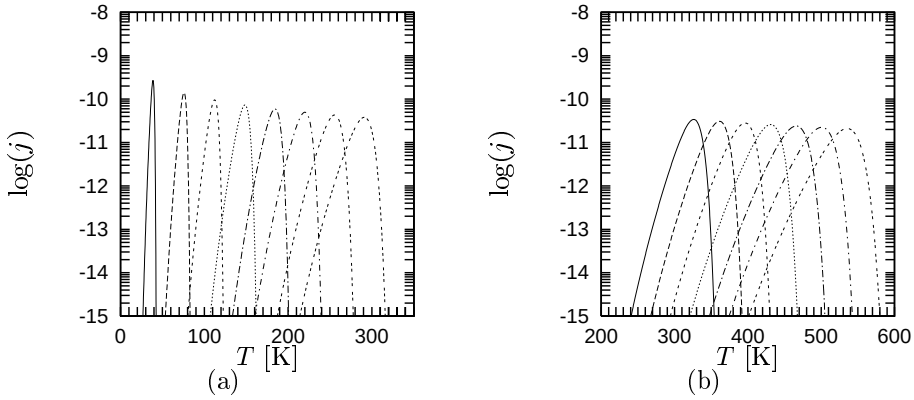

Figure 13. TSD current as a function of temperature for different values of activation energy W (a) when $W = [0.1, 0.2, 0.3, 0.4, 0.5, 0.6, 0.7]$ eV and (b) $W = [0.8, 0.9, 1.0, 1.1, 1.2, 1.3, 1.4, 1.5]$ eV. The curves move to higher temperatures with increasing W-values.

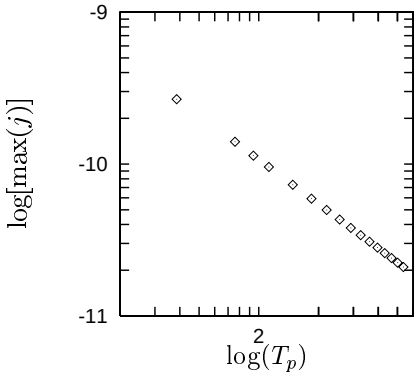

Figure 14. Maximum current value $\max[j(T_p)]$ of a TSD current and its position in the temperature axis T_p for different values of W.

Finally, if the dependencies of logarithm of maximum current values, $\log[j(T_p)]$, and T_p-values on the logarithm of the heating rate, $\log(\mathcal{B})$, were considered, the relationships were linear in both cases, as displayed in Fig. 12, showing the possibility of using the altered heating rates to obtain the activation energy.

2.4. Activation energy

When the activation energy of the conductivity of inclusions W was altered, the largest span of the TSD currents were obtained. The results are presented in Fig. 13. The W-values were assumed starting from 0.1 eV and increasing by steps of 0.1 eV up to 1.5 eV. The shapes of TSD currents were very sharp for low W-values, as presented in Fig. 13a. The TSD current curves became wider as activation energies W were increased as illustrated in Fig. 13b. The peak current $\max[j(T)]$ as a function of peak temperature T_p is presented in Fig. 14. It shows a linear behavior in log-log plot. The dependencies of $j(T_p)$ and T_p on the activation energy W are diplayed in Fig. 15. Both dependencies were proportional to the W-values in the log-log plots.

2.5. Shape factor of inclusions

In this part, the inclusions were assumed to be non-spherical. The shapes were generated using Eqs. (6) and (7). First, the axis-values $x_{1,2,3}$ were chosen to be constant and, later, were assumed to be Gaussian

distributed.

The axis-values and the obtained shape factors in the applied field direction n_1 are presented in Table 1, starting with the spherical-shape as a reference. Then, the shape factor n_1 of ellipsoidal inclusions, which were assumed to be placed with all three principal axes in Cartesian-coordinates, were estimated. $n_{2,3}$-values calculated for the other two directions were the same when the ellipsoidal shape had its principle axis perpendicular to the field direction. Moreover, the highest shape factors were obtained when the principle axes were parallel to the applied field direction. The other cases presented in the table were needle-like shapes with principle axis longer than that of the other two axes. When the needle was parallel to the applied field, the shape factor n_1 increased drastically. However, if the needle was supposed to be perpendicular to the field direction x_1 the n_1-value, as mentioned previously, approached 2. Therefore, for two dimensional simulations with infinitely long cylinders, $n = 2$ is a good approximation. We have also considered oblate-shapes (disks), where they were assumed to be parallel and perpendicular to the applied field. The effect was similar to the needle case when the shapes were parallel to the field direction. However, when they were perpendicular to the applied field direction, the n_1-value was between 1 and 2. In the case when the perpendicular axis-values $x_{2,3}$ were higher than that of the parallel axis x_1 the shape factor approached 1 and the system became a layered-structure.

The simulated TSD current curves with different shape factors are presented in Fig. 16. The solid-line in the figure is the reference TSD current curve for spherical inclusions. In Fig. 16a, TSD current of a system with ellipsoidal shapes parallel to the applied field is presented. Both the current maximum $j(T_p)$ and peak-temperature T_p increased with increasing shape factor. In Fig. 16b, the results obtained for the ellipsoids perpendicular to the applied field are presented. Since the n-value did not alter, the current maximums were all around the same peak-temperature value which was also the same for the reference TSD curve of spherical inclusions. The only difference between the curves was a small perturbation in $j(T_p)$. When the disk-shapes were taken into consideration, as illustrated in Figs. 16c and 16d, the change in the TSD currents were significant when the disks were parallel to the applied field. The TSD currents moved to higher temperatures with increasing shape factor (see Fig. 16c). The current maximums $j(T_p)$ also increased with the shape factor. When the disks were perpendicular to the applied field, unlike the ellipsoidal case (Fig. 16b), the discrepancy between the TSD currents could be distinguished, as shown in Fig. 16d. Note that for disks or needles perpendicular to the applied field, the n_1-values had much less variation than for the inclusions parallel to the applied field.

The change in maximum current $\log[j(T_p)]$ as a function of peak temperature T_p is shown in Fig. 17 when the shape factor n_1 was altered. It was clear that there was a nonlinear functional dependency between them. In the figure, there were two regions where the dependency showed linear tendencies in the semi-logarithm plot, $T_p < 260$ K and $T_p > 260$ K. This behavior was significant if the dependence of T_p-values on n_1 was considered (Fig. 18). The peak-temperature was nearly-constant when $1 < n_1 < 2$, meaning that the change in T_p was not severe. On the other hand if $j(T_p)$ was taken into consideration, the result was the opposite, where the slope was steeper in the same region. For higher values of shape factors, $n > 2$, the slope values of the dependencies were larger for T_p and smaller for $\log[j(T_p)]$, respectively.

2.6. Distribution of shape parameters

An additional problem of greater complexity occures when the inclusion particles have arbitrary shapes, as in ordinary composite materials. Therefore, a closer approach in modeling these materials should introduce distribution of axis-values of ellipsoidal inclusions.

Systems with inclusions having many different shapes were generated, and their TSD currents were calculated. The axis-parameters $x_{1,2,3}$ were chosen from a Gaussian distribution. In the simulations, ten thousand non-interacting particles were considered where at least one of their axis-values were randomly generated [16]

$$\mathfrak{R}^n_{x_i}(m_{x_i}, \sigma_{x_i}) = m_{x_i} + \sigma_{x_i}\mathfrak{R}^n, \tag{9}$$

where $\mathfrak{R}^n$ is a normally distributed deviate with zero mean and unit variance. The parameters m_{x_i} and σ_{x_i} are the mean and variance of the desired normal distribution. Then, the TSD current of each particle in the matrix was calculated and added up to obtain the total TSD current. In Table 2 the mean and variance of the considered shape parameters are shown. In the table, zero varience σ_{x_i} means that the axis-value was

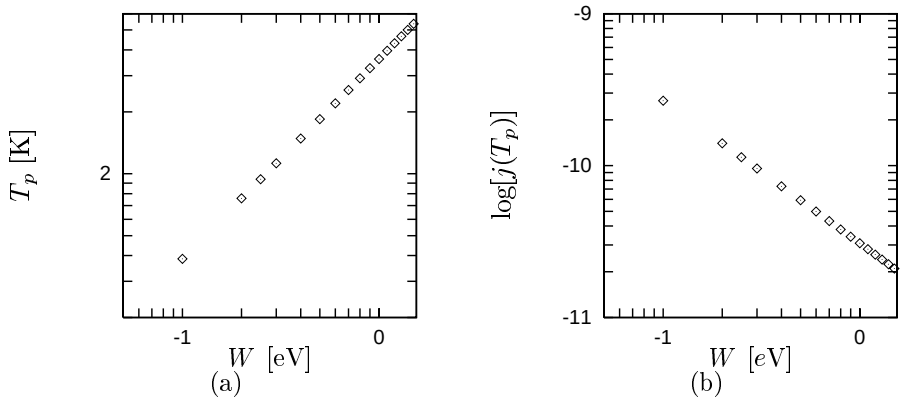

Figure 15. (a) Change in peak temperature T_p as a function of activation energy W of the conductivity process. (b) Maximum current $j(T_p)$ as a function of its position in the temperature-axis T_p for different values of W.

Table 1. Axis-values in arbitrary units and the shape factor estimates.

case	x_1	x_1	x_1	n_1
sphere				
0	1	1	1	3.000
ellipsoid				
1	1	2	1	2.420
2	2	1	1	5.764
3	1	1	2	2.420
needle parallel				
4	5	1	1	17.976
5	10	1	1	49.916
6	50	1	1	839.852
7	100	1	1	3254.785
needle vertical				
8	1	5	1	2.119
9	1	10	1	2.043
10	1	50	1	2.006
11	1	100	1	2.005
disk parallel				
12	2	2	1	4.232
13	5	5	1	8.061
14	10	10	1	14.879
15	50	50	1	132.553
16	100	100	1	483.751
disk vertical				
17	1	2	2	1.897
18	1	5	5	1.334
19	1	10	10	1.165
20	1	50	50	1.055
21	1	100	100	1.049

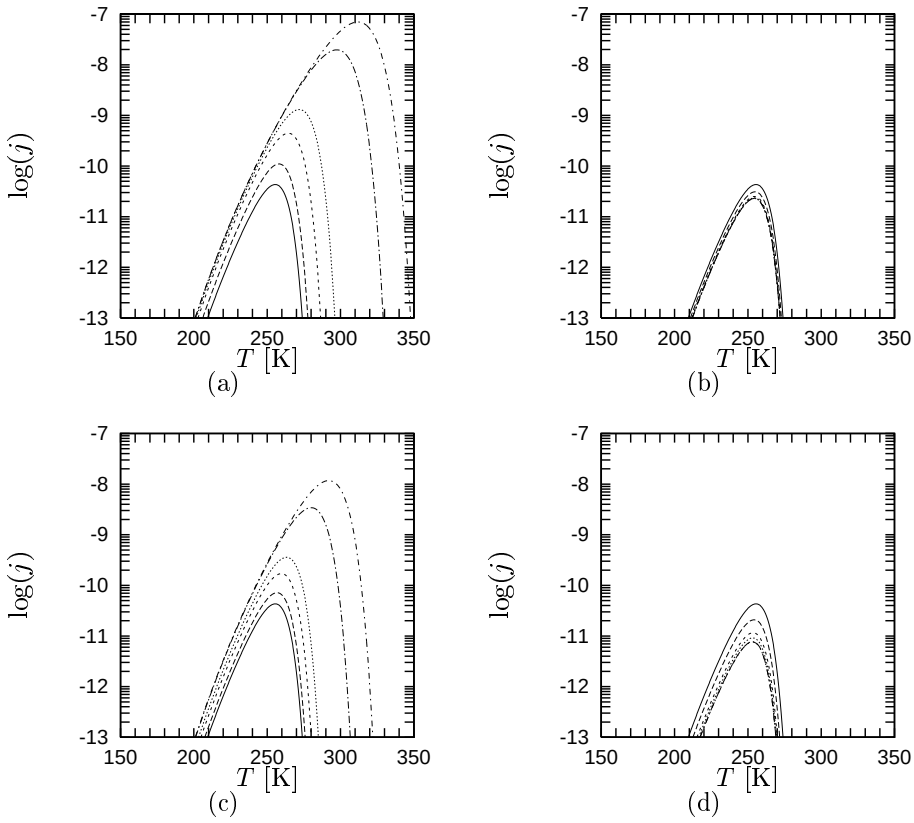

Figure 16. TSD current of different systems with (a) ellipsoids parallel, (b) ellipsoids perpendicular, (c) disks parallel and (d) disks perpendicular to the field direction. The solid-lines are the reference TSD currents for spherical-inclusions. Amplitudes of the curves are increasing with increasing shape factors n_1 see (Table 1).

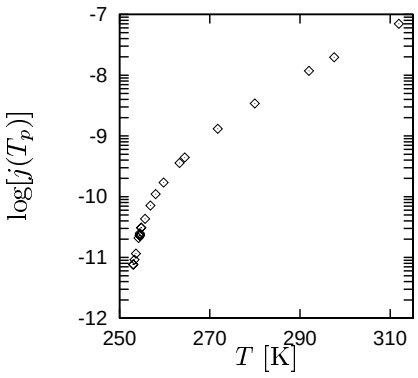

Figure 17. The current maximum $j(T_p)$ as a function of peak temperature T_p when shape factor n_1 was altered from that of a sphere.

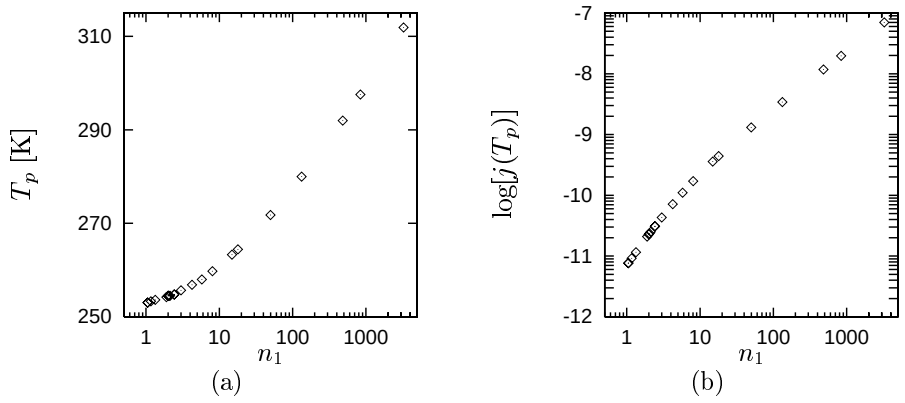

Figure 18. Dependences of peak temperature T_p and logarithm of current maximum $j(T_p)$ as a function of shape factor n_1.

not distributed, but it was taken to be constant: $\Re^n_{x_i}(m_{x_i}, 0) = m_{x_i}$. The shape factor n was then calculated in the applied field direction x_1. The case 0 was the reference TSD current for spherical inclusions. First, perturbed spherical shapes were considered which are the cases 1 and 2 in the table. Then, disk-like shapes (cases 3 and 4) were generated. Finally in case 5, all the axis-values were distributed. The ratio of the axis-values and their variances were also increased (cases 6-15).

In Fig. 19 shape factors n_1 as a function of distributed axis and axes are presented. Only the dependency of n_1 on x_1 and x_2 directions were considered, and since the volume of the inclusions did not play any role in the calculations, as the axis-values were normalized to x_3. The n_1-values obtained from case 1 in Table 2 are labeled ab I in the figures. In the same way, the n_1-values obtained from case 2 are presented in the figures and they are labeled as II. Moreover, the spherical shape factor is also illustrated as a horizontal-line at $n_1 = 3$ in the figures. The distributed points in the figures a-b and c-d are for the cases 3 and 4, respectively. When case 3 was considered, the $n_1(x_1/x_3)$-values, as shown in Fig. 19a, demostrated a similar tendency as case 2 but the results spread. This behavior exhibited that the inclusions were needle-like in the field direction. However, if the same shape factors n_1 were plotted against the other normalized axis-value, x_2/x_3 (Fig. 19b), unlike the previous distribution, there were no correlations between the axis-values and the curves labeled with I and II. This result showed that the influence of the perpendicular axis on the shape factor was not significant. The n_1-values of the other considered case in which the x_1-value was kept constant and the other two axis-values were distributed (case 4), are presented in Fig. 19c and Fig. 19d. Since the axis-values were normalized to x_3, one could expect similar behavior as in case 3, however, the distributed n_1 values were not exactly aligned with direction II. The spread was wider and the orientation was different. Much surprisingly, when the shape factor was plotted against the normalized x_2-axis, the distribution was horizontal-like spreading around the spherical shape factor as presented in Fig. 19d.

When all the axis-values are distributed, the shape factor is presented in Fig. 20. Once again subplots (a) and (b) show the shape factor n_1 as a function of the normalized axis-values of $\Re^n_{x_1}(1, 0.1)/\Re^n_{x_3}(1, 0.1)$ and $\Re^n_{x_2}(1, 0.1)/\Re^n_{x_3}(1, 0.1)$, respectively. The labels I and II are the same as in the previous, Fig. 19. The behavior in Fig. 20a is similar in shape to the behavior in Fig. 19a, but spread on a wider region. It is also similar behavior if Fig. 20b and Fig. 19b were compared. As a result, if all the axis-values are distributed over a narrow range, there is not that much difference in the shape factors between case 5 and cases 1-4 in Table 2. This is presented in Fig. 21a. The n_1-values were distributed but the variance of the distributions were alike. The TSD current curves of the corresponding cases were the same as that of the spherical inclusions, (see Fig. 21b).

A similar approach was extended to needle-like shapes which were parallel and perpendicular to the field-axis. The calculated shape factors are shown in Fig. 22. The graphs display the extentions of curves I and II in Fig. 19 where the axis-values were distributed over a wider range. In fact, the curves were obtained using cases 1, 6 and 11, and cases 2, 7 and 12 in Table 2 for Fig. 22a and Fig. 22b, respectively. As expected,

Table 2. Axis-values in arbitrary units where the values of m_{x_i} and σ_{x_i} are used in Eq. 9.

case	$m_{x_1} - \sigma_{x_1}$	$m_{x_2} - \sigma_{x_2}$	$m_{x_3} - \sigma_{x_3}$
0	1 – 0.0	1 – 0.0	1 – 0.0
1	1 – 0.0	1 – 0.1	1 – 0.0
2	1 – 0.1	1 – 0.0	1 – 0.0
3	1 – 0.1	1 – 0.1	1 – 0.0
4	1 – 0.0	1 – 0.1	1 – 0.1
5	1 – 0.1	1 – 0.1	1 – 0.1
6	1 – 0.0	5 – 1.0	1 – 0.0
7	5 – 1.0	1 – 0.0	1 – 0.0
8	5 – 1.0	5 – 1.0	1 – 0.0
9	1 – 0.0	5 – 1.0	5 – 1.0
10	5 – 1.0	5 – 1.0	5 – 1.0
11	1 – 0.0	10 – 2.0	1 – 0.0
12	10 – 2.0	1 – 0.0	1 – 0.0
13	10 – 2.0	10 – 2.0	1 – 0.0
14	1 – 0.0	10 – 2.0	10 – 2.0
15	10 – 2.0	10 – 2.0	10 – 2.0

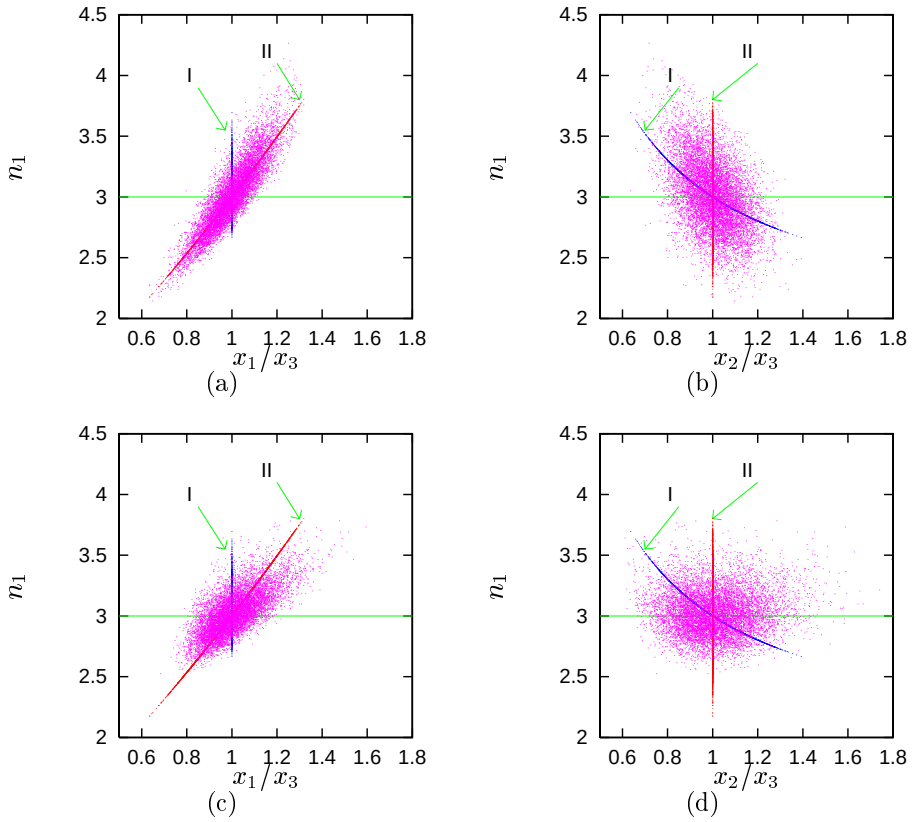

Figure 19. Shape factor n_1 as a function of distributed axis-values $\mathfrak{R}^n_{x_i}(m_{x_i}, \sigma_{x_i})$. The distributions labeled by I and II are for case 1 and 2 in Table 2 where $x_{1,3}$ and $x_{2,3}$ are fixed, respectively. The horizontal line is the shape factor for spherical incslusions $n_1 = 3$. The points represent (a) n_1 as a function of x_1/x_3 for case 3, (b) n_1 as a function of x_2/x_3 for case 3, (c) n_1 as a function of x_1/x_3 for case 4, and (d) n_1 as a function of x_2/x_3 for case 4.

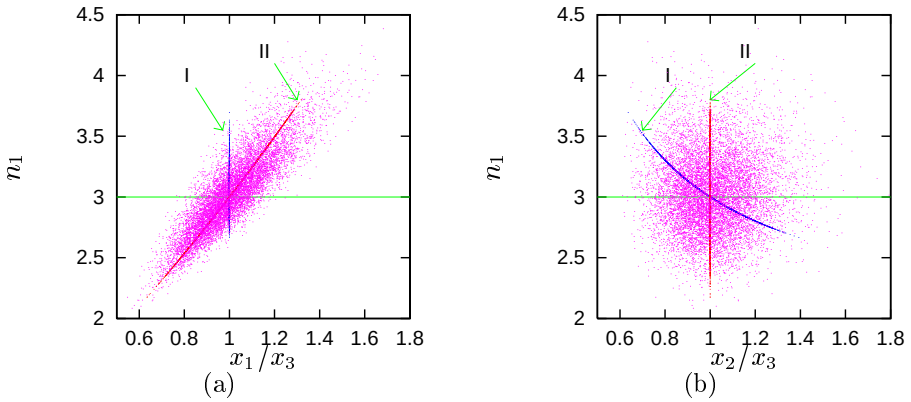

Figure 20. The shape factor as a function of normalized (a) x_1 and (b) x_2, when all the axis-values were distributed.

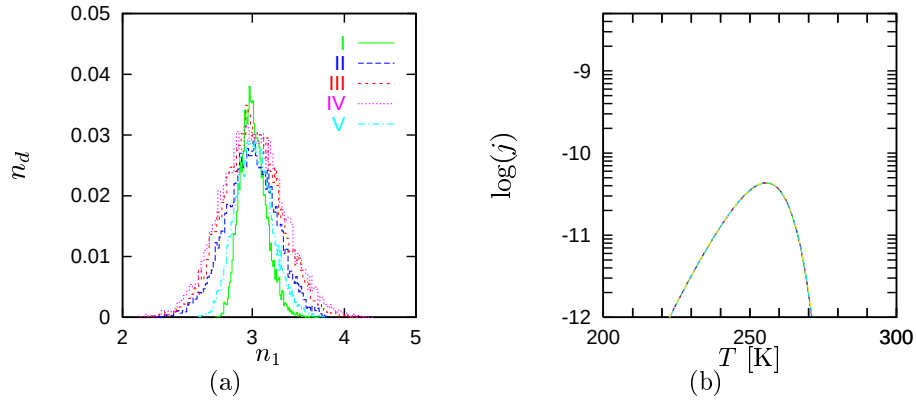

Figure 21. (a) The number density of shape factors obtained in the simulations with different axis distributions. The labels represent the cases in Table 2. (b) TSD currents of the corresponding cases converging to the same curve.

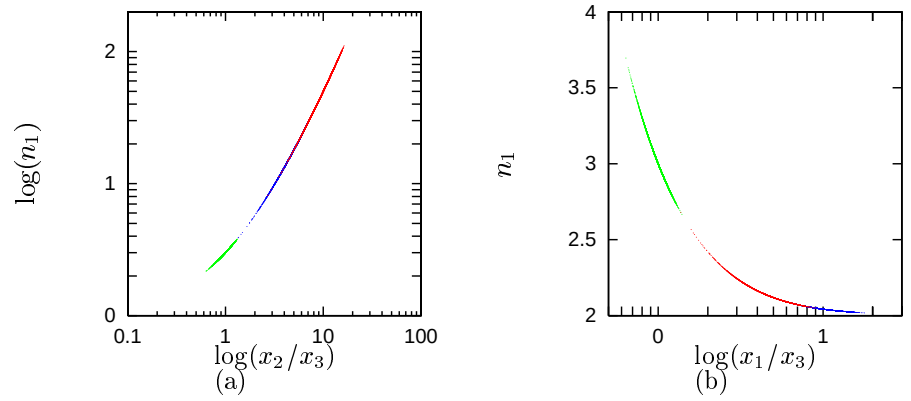

Figure 22. The shape factor as a function of distributed (a) x_1 (b) x_2-values while the other two axis were kept constant.

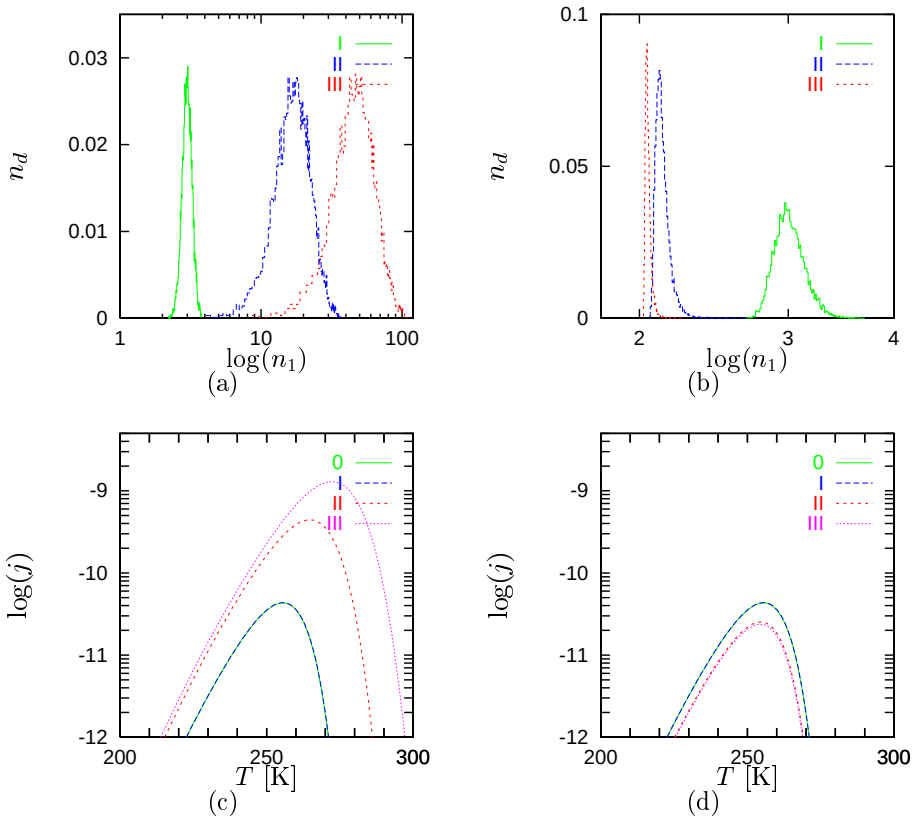

Figure 23. Shape factor density distribution for needdle-like shapes (a) perpendicular and (b) parallel to the field direction. (c) and (d) show the calculated TSD current curves together with the TSD current curve of spherical inclusions case. The labels 0, I, II and III at (a) and (c) corresponds to cases 0, 1, 6 and 11, and the labels 0, I, II and III at (b) and (d) corresponds to cases 0, 2, 7 and 12 in Table 2, respectively.

when the normalized x_2-values became larger than the other two axis-values, the shape factor was cylindrical and approached to 2. On the other hand, if the normalized x_1 value was taken larger than that of the other two axes, the shape factor increased linearly in a log-log scale. When the x_1/x_3 was small, the shape factor approached to one, meaning the inclusions were disk-like. The number density of shape factors n_d as well as the corresponding TSD currents are displayed in Fig. 23. Again, when the inclusions were aligned with the applied field, the influence of the shape factor on the TSD current was significant.

When cases 6-15 in Table 2 were considered, the n_1-values definitely influenced the TSD current curves. The shape factor number density n_d distributions and the calculated TSD current-responses are presented in Fig. 24. The maximum-current $j(T_p)$ as a function of peak-temperature T_p was also investigated and is shown in Fig. 25. The behavior was similar in shape as that in Fig. 17.

3. TSD currents of interacting inclusions in two-dimensions

3.1. Modeling procedure

Analytical calculations of electromagnetic problems using Maxwell's equations are limited to geometrical constraints. For some simple geometries with a small number of materials (regions) and symmetries, analytical solutions can be using methods of images, orthogonal functions (Green functions) and complex variable techniques (conformal mapping) [17, 18, 19, 20, 21]. The conformal mapping can only be applied to two-dimensional problems in which the third spatial axis is neglected. For more complex geometries and

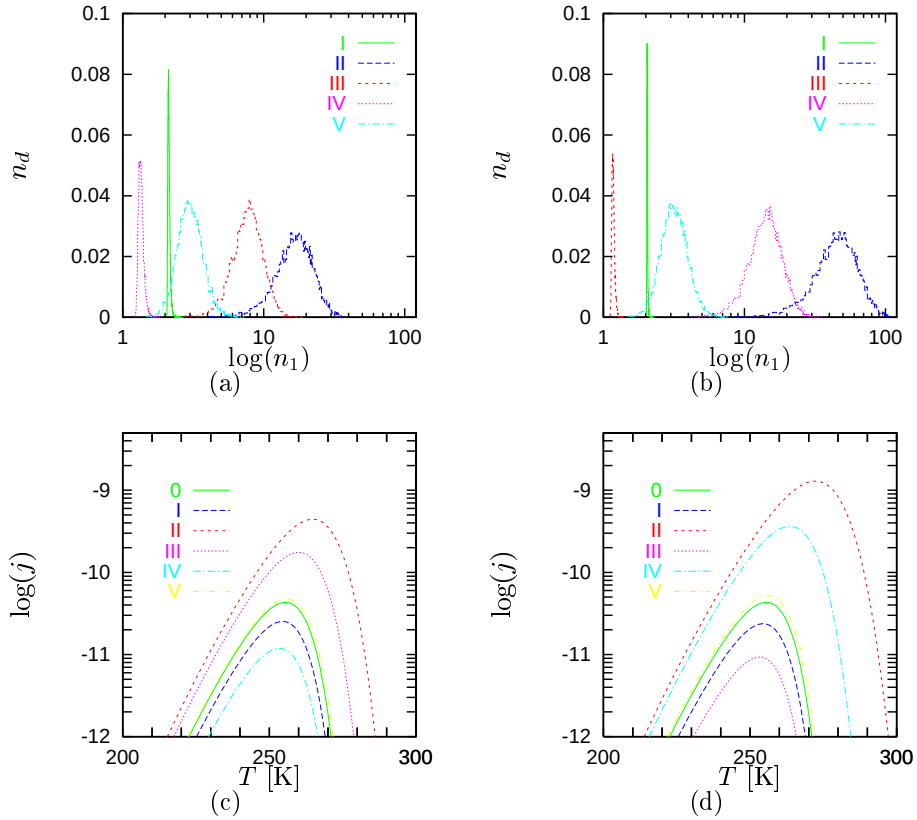

Figure 24. Density of shape factors for (a) cases 6 to 10, and (b) cases 11 to 15 in Table 2. The corresponding TSD current curves (c) for figure* (a) and (d) for figure* (b), respectively. The labels represent the cases 6 through 10 in figure* (a) and 11 through 15 in figure* (b). The label 0 is the reference TSD current of spherical inclusions.

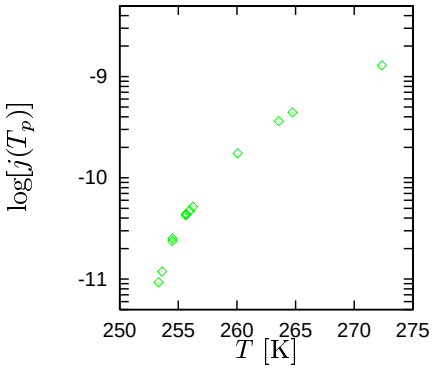

Figure 25. Maximum current value, $\max[j(T)]$ as a function of peak temperature for different shape factors, n_1, obtained by distributing inclusions on axis parameters.

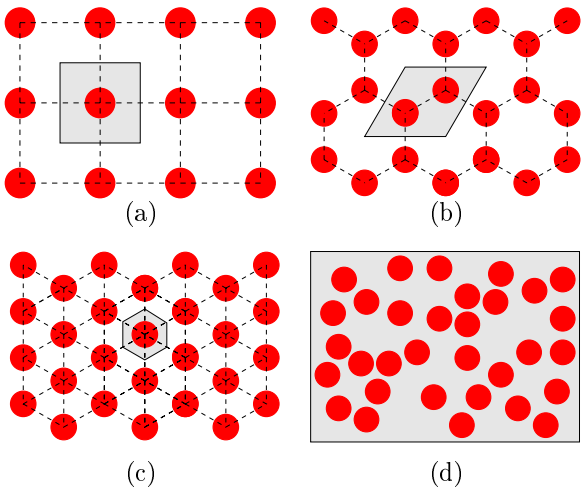

Figure 26. (a) Square, (b) honeycomb, (c) hexagonal and (d) random structures. Dark circles are the inclusions which are distributed in the host medium. The shaded areas are the primitive cells which are used in the calculations.

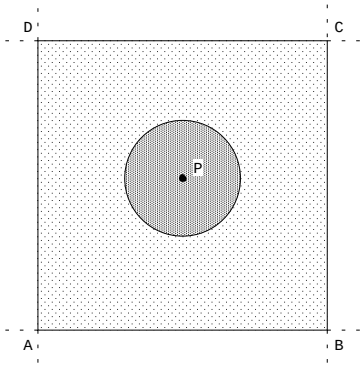

Figure 27. The unit-cell of square lattice with corners at $ABCD$ used in the calculations. Dark region is the disk inclusion with ε_2 and σ_2 and the lighter region is the matrix media with ε_1 and σ_1.

non-homogeneous regions composed of several materials, numerical solutions of partial differential equations and of integral equations have been developed [22], *e.g.*, the finite difference method, the finite element method (FEM), the method of moments and the boundary element method, etc.

The frequency dependent complex dielectric permittivity $\varepsilon(\omega)$ of a binary system composed of monodispersed conductive cylindrical inclusions in a less conductive matrix can be calculated using the FEM [23, 24]. Indeed, the influence of the electrical properties of constituents and the concentration of inclusions on $\varepsilon(\omega)$ can be simulated and investigated effortlessly. Here, initially, we concentrated on regularly distributed systems, composed of infinitively long-and parallel to one another cylindrical inclusions in a host medium. The interfacial polarization was studied by considering square, honeycomb and hexagonal structures in two dimensions (Fig. 26). The regular distribution of inclusions in a composite is, so far, not realistic; however, the information obtained from calculations provides an interesting case study and is a good way to compare numerical approaches with those of analytical solutions. Random distribution of inclusions should be more realistic since the distribution within real composites is normally highly irregular, therefore, random structures were also included and examined.

The regular structures were chosen for symmetry reasons in the FEM calculations (all the lattices, except for the honeycomb types, lattices with a basis in two dimensions). The two-dimensional honeycomb structure

(Fig. 26b) is not a lattice with a single-point basis, but can be presented as a lattice with a two point basis [25]. In order to use two dimensional calculations, surfaces were considered to be perpendicular to the direction of the cylindrical inclusions in the structures, as shown in Fig. 26. Furthermore, in these structures the smallest repeatable units, primitive cells (shaded regions in Fig. 26), were taken into consideration. Such an approach allows for an easier assignment of boundary conditions for calculating the potential field distribution. We have considered the expected equi-electric and equi-potential field lines on the outer boundaries of the primitive cells, should be constant [22, 26]. The unit cell approach was used in which the boundaries of the unit cell were equi-potential or electric field lines [27, 28]. It is worth mentioning that the geometrical model in two dimensions may work for three dimensions just by considering the interaction between the cylinders which can be similar as between spherical inclusions in three dimensions [29].

3.2. Numerical calculations

Numerical solutions of electrostatic problems within a non-conducting medium are based on solving Poisson's equation

$$\nabla \cdot (\varepsilon\varepsilon_0 \nabla\phi) = -\rho, \tag{10}$$

where ϕ, ε, and ρ denote the electrical potential, the permittivity of the medium and the total charge in the considered region, respectively. ε_0 is the permittivity of free space, $\varepsilon_0 = 1/36\pi$ pF/m. However, if the medium is conductive where no free charges and sources of charges are allowed, then the solution is given by

$$\nabla \cdot (\sigma\nabla\phi) = 0 \tag{11}$$

where σ is the conductivity of the region. When the medium is a mixture of these two cases, it consists of dielectric and conductive components. The solution is then given by a time dependent and complex electric potential in the region with the coupling of Eqs. (10) and (11):

$$\nabla \cdot (\sigma\nabla\phi) + \nabla \cdot \left[\frac{d}{dt}(\varepsilon\varepsilon_0\nabla\phi)\right] = 0 \tag{12}$$

or equivalently,

$$\nabla \cdot [(\sigma + \imath w\varepsilon\varepsilon_0)\nabla\phi] = 0, \tag{13}$$

where no free charges are assumed in the region. The last set of equations consists of the continuity and Laplace equations for a medium with a complex dielectric constant.

We have used a field calculation software called 'ACE' [24] based on FEM. As an example, the unit cell of the square lattice is presented in Fig. 27. The boundary conditions were chosen as follows for this particular structure: along line $[AB]$ the potential was 0 V_{rms} level, along line $[CD]$ it was 1 V_{rms}. The lines $[AD]$ and $[BC]$ in the figure were symmetry lines in which the units were assumed to be repeating in those directions. The calculations were performed under steady-state periodic conditions. Similar procedures were also used in the other considered structures in which boundary conditions were applied to the outer boundaries of the unit-cells. In the FEM, the region of interest (computation domain) is divided into triangles via adiscretization procedure also known as meshing. We have used an adaptive meshing technique which is based on the change of the dielectric displacement vector in the domain. In order to obtain a reliable solution, linear, quadratic and cubic solution sets were compared, and the results of the cubic solutions were taken due to the smoothness of the resulting potential distribution.

After obtaining the potential distribution in the domain, the complex dielectric permittivity of the medium is calculated. The complex permittivity of a heterogeneous medium can be calculated in several ways, *e.g.*, by using Gauss' law and losses, using the averages of dielectric displacement $\langle \mathbf{D} \rangle$ and electric field $\langle \mathbf{E} \rangle$, and using the total current density $\mathcal{J}$ and the phase difference θ. Here, the latter approach was used.

Table 3. Structures, their relaxation times and dielectric strengths.

Structure	τ (ms)	$\Delta\varepsilon$
Classical	4.44	3.20
Hexagonal	6.15	4.36
Square	6.15	5.22
Honeycomb	6.96	5.36
Random	6.43	5.70
	7.28	6.62
	7.61	6.55
	6.65	6.22

The root mean square value of the total current density and the phase are obtained from the software [24]. Therefore, the complex dielectric permittivity is expressed as

$$\varepsilon(\omega) = \frac{\mathcal{J}}{C_0 V_0 \omega}[\sin(\theta) - \imath\cos(\theta)], \tag{14}$$

where C_0 and ω are the geometrical capacitance and the angular frequency. V_0 is the potential difference between the voltage-applied sides.

In the previous section, non-interacting inclusions in three-dimensions were considered when the concentration of the inclusions q were 0.1, in which the mutual interaction of inclusions can be neglected. In these numerical calculations by means of FEM, cylindrical inclusions were assumed, with $n = 2$, and accordingly, two-dimensional field calculations were performed as presented in [30]. In the calculation, influences of not only higher concentrations of inclusions but also their distributions were investigated.

3.3. Isothermal dielectric responses

In numerical calculations relative dielectric constants of two media were taken to be the same, $\varepsilon_{1,2} = 4$. The reason to choose them equal was that, at optical frequencies dielectric constant of the composite structures, ε_∞ had the same relative permittivity as the two media. The conductivity of the host medium was taken to be 10^{-20} S/m in order to assume that it was insulating. Conductivity of cylindrical inclusions σ_2 was 10^{-7} S/m, and the concentration of inclusions q was 0.4. It was found that dielectric permittivities of the structures ε' with different inclusion distribution were different, although the inclusion concentration was the same. This could not be obtained by classical theories.

The dielectric responses ε'obtained from field calculations and classical model [4] are presented in Fig. 28a. The dielectric strength $\Delta\varepsilon$ of regular structures due to the interactions between the inclusions were higher than that resulting from the classical model. Highest $\Delta\varepsilon$ was obtained for honeycomb structure, and it was followed by square and hexagonal structures. Moreover, four random structures were also considered in the numerical calculations. It was observed that the random structures had even higher dielectric strengths $\Delta\varepsilon$ than the regular structures. The $\Delta\varepsilon$-values are shown in Table 3. The real parts of the dielectric permittivities ε' are presented in Fig. 28a. The individual responses of random structures spread over a region in permittivity-axis that did not converge to a single static dielectric constant ε_s. Relaxation times τ were calculated by taking the second derivative of $\log\varepsilon'(\omega)$ with respect to angular frequency $\log\omega = 2\pi\nu$ two times. These values together with the dielectric strengths $\Delta\varepsilon$ are also presented in the table. The relaxation time τ for the classical model was lower than that of the considered structures.

3.4. Thermally stimulated depolarization currents

In TSD current calculations for all the considered structures, the applied electric field E and activation energy W were assumed to be constants; $E = 10$ V/m and $W = 0.5$ eV. Structure dependent parameters *i.e.* relaxation time τ and dielectric strength $\Delta\varepsilon$ were taken from the dielectric responses in isothermal

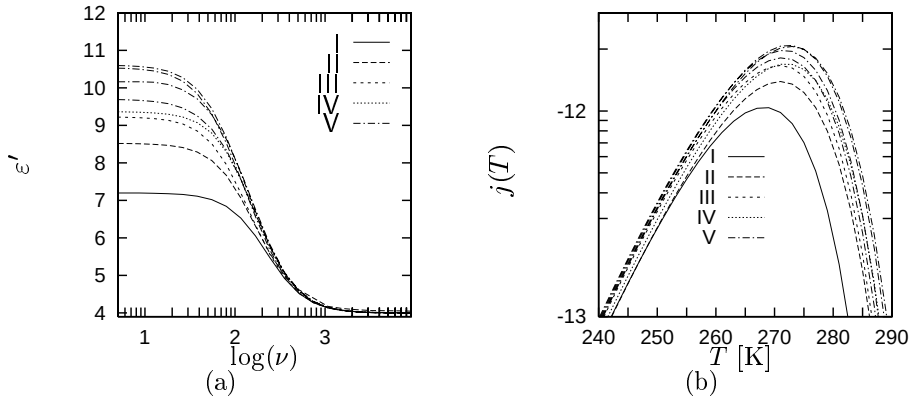

Figure 28. (a) Real part of the relative dielectric constant of the structures as a function of frequency. (b) TSD currents of the structures. The labels I, II, III, IV and V represent classical [4], hexagonal, square, honeycomb and random structures, respectively.

conditions, Table 3. The pre-exponential factors were calculated using the relaxation times τ presented in Table 3. It was assumed that the τ-values were Arrhenius activated and were observed at $\sim$ 300 K. It was, furthermore, assumed that the structures were polarized completely with the applied field. The linear heating rate of the TSD current $\mathcal{B}$ was 5 K/min. The resulting TSD currents, using Eq. (4), are presented in Fig. 28b. The current peak-temperatures T_p were distributed around 275 K for all the structures. The TSD current from the classical model had a lower peak temperature value $T_p \sim 270$ K. The main difference between the TSD current curves was in the peak-current $j(T_p)$ which is directly proportional to the dielectric strength $\Delta\varepsilon$ of the structures. Again, just like for the isothermal dielectric responses, the TSD currents of the random structures had higher values than those of the other structures.

3.5. Discussion on higher filler concentrations

Isothermal dielectric responses and TSD currents were calculated for the structures containing 40% inclusions. It was observed that the four considered random structures had higher dielectric strengths $\Delta\varepsilon$ and TSD current values $j(T)$ than both the other regular and classical structures. Moreover, dielectric permittivities and TSD currents of the random structures did not converge to a common value or showed a common behavior. It was also realized that it was not an easy task to model and understand the dielectric behaviour of composite systems with higher concentration of inclusions; since, depending on the spatial distribution of inclusions, different dielectric properties can be achieved.

4. Conclusion

In the calculations, a model based on a single-thermally-activated process, together with the conductivity of the inclusions, was used. Moreover, the matrix medium was assumed to be insulating. Altering only one parameter at a time, its influence on the TSD currents was investigated. Even the shape of inclusions has influenced the TSD currents. Therefore, it would be possible to obtain information on micro-structure of composites using the TSD current technique. However, if the inclusions were perturbed spherical shapes, there were no differences between the TSD spectra.

We have compared two methods previously proposed in the literature to estimate the activation energy of a thermally stimulated process, and have showed that the activation energy estimates calculated from the logarithm of the TSD current versus inverse normalized termperatures, are more accurate than calculating the activation energy using altered heating rates and temperatures in which the maximum currents are observed.

The considered systems were assumed to be totally polarized; therefore, it was not possible to use the other experimental parameters than the heating rate in TSD current technique, such as polarizing voltage and polarization temperature. Introducing those parameters would make it possible to obtain more information on materials and their electrical properties.

Using the FEM field calculations in isothermal conditions, it was possible to investigate the TSD currents in binary composite mixtures with high concentration of inclusions in which particle-particle interactions played an important role in the resulting dielectric properties. The random structures showed higher polarization amplitutes than the regular structures. However, in this approach, just like in the considerations in the second section, a single-thermally-activated process was assumed. The simulations could be expanded where both conductivities and dielectric permittivities of the inclusions and the matrix would be temperature dependent.

Finally, in order to know much more about the physics and the processes involved in the TSD current, more simulations and measurements on well-defined systems should be performed.

Acknowledgement

This work was a part of the intermediate doctorate degree (teknisk licenciatexamen) report that was presented on 17 April, 2000 at Chalmers University of Technology, Gothenburg Sweden.

References

[1] R. Landauer, Electrical conductivity in inhomogeneous media, in: J.C. Garland, D.B. Tanner (Eds.), Electrical Transport and Optical properties of Inhomogeneous Media, Vol. 40 of AIP Conference Proceedings, American Institute of Physics, New York, 1978, pp. 2–43.

[2] D.K. Hale, The physical properties of composite materials, Journal of Materials Science 11 (1976) 2105–2141.

[3] F. Lux, Review models proposed to explain the electrical conductivity of mixtures made of conductive and insulating materials, Journal of Materials Science 28 (1993) 285–301.

[4] R. Sillars, The properties of a dielectric containing semiconducting particles of various shapes, Journal of Institution of Electrical Engineers 80 (1937) 378–394.

[5] E. Tuncer, S.M. Gubański, Dielectric properties of different composite structures, in: A. Wlochowicz, E. Targosz-Wrona (Eds.), Dielectric and Related Phenomena DRP'98: Polymers and Liquid Crystals, Vol. 4017 of Proceedings of SPIE, Technical University of Lodz, Branch in Bielsko-Biala, Poland, SPIE, The International Society for Optical Engineering, Washington, 1998, pp. 136–142.

[6] B. Sareni, L. Krähenbühl, A. Beroual, C. Brosseau, Effective dielectric constant of random composite materials, Journal of Applied Physics 81 (5) (1997) 2375–2383.

[7] C. Bucci, R. Fieschi, Ionic thermocurrents in dielectrics, Physical Review 148 (2) (1966) 816–823.

[8] P. Muller, Electric relaxation currents in high-resistivity solids, Physica Status Solidi (a): Applied research 67 (1981) 11–60.

[9] J. van Turnhout, Thermally stimulated discharge of polymer electrets, Tech. Rep. Comm. No 471, Central Laboratorium, Delft, The Netherlands (1972).

[10] R. Vila, M.J. de Castro, Thermally stimulated depolarization of ellipsoidal particles in an insulating medium, Journal of Physics D: Applied Physics 25 (1992) 1357–1364.

[11] J.C. Maxwell, A Treatise on Electricity and Magnetism- Volume 1, 3rd Edition, Clarendon Press, Oxford, 1891, reprint by Dover.

[12] K.W. Wagner, Zur theorie der unvollkommenen dielektrika, Annalen der Physik 40 (5) (1913) 817–855.

[13] P. Debye, Polar Molecules, Dover Publications, New York, 1945.

[14] H. Fricke, The Maxwell-Wagner dispersion in a suspension of ellipsoids, Journal of Physical Chemistry 57 (1953) 934–937.

[15] A.H. Booth, Calculation of electron trap depths from thermoluminescence maxima, Canadian Journal of Chemistry 32 (1954) 214–215.

[16] W.H. Press, S.A. Teukolsky, W.T. Vetterling, B.P. Flannery, Numerical Recipies in C: The Art of Scientific Computing, 2nd Edition, Cambridge University Press, Cambridge, 1992, Ch. 7. Random Numbers, pp. 287–288.

[17] R.S. Elliot, Electromagnetics, McGraw-Hill Book Company, New York, 1966.

[18] K.-H. Steiner, Interactions between Electromagnetic Fields and Matter, Vol. 1 of Vieweg Tracts in Pure and Applied Physics, Pergamon Press, Oxford, 1973.

[19] S. Ramo, J.R. Whinnery, T. van Duzer, Fields and Waves in Communication Electronics, 3rd Edition, Wiley, New York, 1994.

[20] L. Eyges, The Classical Electromagnetic Field, Dover, New York, 1972.

[21] E. Weber, Electromagnetic Theory: Static Fields and Their Mappings, Dover Publications Inc., New York, 1965.

[22] J.R.C. Richard, Computational Methods for Electromagnetics and Microwaves, John Wiley & Sons, Inc., New York, 1992.

[23] P.P. Silvester, R.L. Ferrari, Finite Elements for Electrical Engineers, 2nd Edition, Cambridge University Press, Great Britain, 1990.

[24] Asea Brown Boveri Corporate Research, Västerås Sweden, Ace 2.2 Users Manual and Ace Command Language Reference (1993).

[25] N.W. Arshoft, N.D. Mermin, Solid State Physics, international Edition, Saunder College Publishing, Orlando, USA, 1976.

[26] T.H. Hubbing, Survey of numerical electromagnetic modeling techniques, Tech. Rep. TR91-1-001.3, University of Missouri-Rolla, Electromagnetic Compatibility Laboratory (1991).

[27] L. Rayleigh, On the influence of obstacles arranged in rectangular order upon the properties of a medium, Philosophical Magazine 34 (1892) 481–502.

[28] Y.P. Emets, Electrical characteristics of three-component dielectric media, Journal of Experimental and Theoretical Physics 87 (3) (1998) 612–620.

[29] M. Plischke, B. Bergersen, Equilibrium Statistical Physics, 2nd Edition, World Scientific, London, 1994.

[30] E. Tuncer, S.M. Gubański, B. Nettelblad, Dielectric relaxation in dielectric mixtures: Application of the finite element method and its comparison with mixture formulas, Journal of Applied Physics 89 (12) (2001) 8092–8100.